Journal of Materials Science: Materials in Electronics (2018) 29:10933–10941
https://doi.org/10.1007/s10854-018-9171-4

The effects of high-energy ball milling on the synthesis, sintering and microwave dielectric properties of Li_2TiO_3 ceramics

Somaye Ghaffari[1] · Touradj Ebadzadeh[1] · Masoud Alizadeh[1] · Keivan Asadian[2] · Yadolah Ganjkhanlou[3] · Mohammad Saleh Shafeeyan[4]

Received: 21 January 2018 / Accepted: 22 April 2018 / Published online: 21 May 2018

Abstract
The effect of high-energy ball milling (HEBM) on the synthesis and sintering of Li_2TiO_3 was investigated. XRD Phase analysis of milled powders revealed a common phenomenon of peak broadening due to crystallite size reduction and loss of long-range periodicity. Thermal analysis results showed that the formation of Li_2TiO_3 can be facilitated with high-energy ball mill. Density measurement of sintered parts revealed that milling time of 5 h (HEBM-5) is sufficient to achieve a high density of 3.19 g/cm^3 (93.82% of the theoretical density) at low sintering temperature of 1100 °C. The average particle size of synthesized Li_2TiO_3 powder was about 150 nm. SEM observations revealed the achievement of dense microstructures with abnormal grain growth. Optimal dielectric constant of $\varepsilon_r = 21.85$, $Q \times f = 17510$ GHz and τ_f value of +26 ppm/°C were achieved. Li_2TiO_3 was also synthesized without high-energy milling and sintered at 1100 °C and the density of 3.03 g/cm^3 (89.11% of theoretical density) was achieved.

1 Introduction

In recent years, the Information Communications Technology (ICT) has progressed in areas like Internet of Things (IoT) technology, microwave telecommunications, Direct-broadcast satellite television (DBS TV), satellite broadcasting, Intelligent Transport Systems (ITS) and Industry 4.0 which promoted scientific research of new materials [1–5]. Microwave dielectric materials applied in dielectric resonators, filters, substrates, etc. play a key role in communication system [6–10]. Li_2TiO_3 ceramic is one of the members of the ternary rock salt oxide ceramic systems that have been reported to have excellent microwave dielectric properties [11–16]. Li_2TiO_3 possesses high quality factor ($Q \times f > 15{,}000$ GHz for pure Li_2TiO_3) [17–19] and moderate dielectric constant (22) [15]. The synthesized powders are usually characterized by a large grain size and inferior sinterability [18]. In addition, porous microstructure due to sublimation of lithium [19, 20] and crack formation due to phase transition under high sintering temperatures (above 1150 °C) [19, 21] adversely affect the densification of Li_2TiO_3 and therefore reducing the sintering temperature is very important to control the above-mentioned defects. Several approaches have been generally applied to enhance the sintering characteristics of ceramics such as addition of dopants [22–25], addition of sintering aids with low melting points [26–29], using wet chemistry synthesis methods (hydrothermal, sol–gel,…) [30–33] and modified solid state reaction methods like high-energy ball mill [34, 35]. Two last approaches have been attractive as a consequence of nanopowders production capability which provide powders with high surface area and stored energy that enhance solid state densification at lower temperatures [36–39]. Because sol–gel routes can be tedious and often require toxic and/or expensive reactants, it seems that the high-energy ball mill is an enhanced approach to synthesis of materials [40]. For practical applications, high-energy ball mill is the most

✉ Touradj Ebadzadeh
t-ebadzadeh@merc.ac.ir

✉ Mohammad Saleh Shafeeyan
ms.shafeeyan@gmail.com

[1] Department of Ceramics, Materials and Energy Research Center, P.O. Box 31787-316, Karaj, Alborz, Iran

[2] Department of Semiconductors, Materials and Energy Research Center, P.O. Box 31787-316, Karaj, Alborz, Iran

[3] Department of Physical Chemistry, Faculty of Chemical Technology, University of Pardubice, Studentska 573, 532 10 Pardubice, Czech Republic

[4] Department of Chemical Engineering, Golestan University, Gorgan, Iran

widely used since it is easy to scale-up, and the precursors are cheap and abundant [41].

In the present work, the synthesis of Li_2TiO_3 fine powders through a solid state reaction from high-energy ball milled Li_2CO_3 and TiO_2 mixtures has been reported. Furthermore, the characteristics of synthesized powder and sintered parts were examined using XRD, FE-SEM, Raman spectroscopy, BET, PSA, and TG–DTA. The effect of high-energy milling on the microstructures, densification behavior and microwave dielectric properties of Li_2TiO_3 ceramics was also investigated.

2 Materials and methods

Li_2CO_3 (Sigma Aldrich, 13,010, 99% purity) and TiO_2 (Merck, 1.00808.1000, > 99% purity) were used as starting materials. High-energy ball milling (HEBM) was performed in a PM 400 Retsch planetary ball mill using 250 mL tungsten carbide vials with diameter of 7.5 cm and height of 7.2 cm and tungsten carbide balls with 10–20 mm diameter at 300 rpm. The ball-to-powder ratio of 10:1 was chosen for different milling times of 1, 5, 10 and 15 h denoted as HEBM-1, HEBM-5, HEBM-10 and HEBM-15, respectively. The relative speed of vials and disk was − 2.5. Low-energy ball milling (LEBM) was also carried out in a planetary ball mill using a polyethylene vial and zirconia balls in 99.97% pure ethanol and the sample were denoted as LEBM.

The particle size of as-received powders after high-energy mill was measured by Fritsch Particle Sizer analysette. Milled powders were calcined in an electrical box furnace at different temperatures of 500, 550, 600, 700 and 800 °C with 4 h holding time at maximum temperature and heating rate of 5 °C/min.

The surface area of prepared powders was determined by means of nitrogen adsorption at − 196 °C using an automated gas adsorption analyser (GEMINI 2375, Micromeritics, USA). The mean particle size (D) was estimated using the following equation (Eq. 1)

$$D = 6/s \times \rho \quad (1)$$

In which 's' is the BET surface area (m^2/g) and 'ρ' is the powder density (kg/m^3) [42]. The density of synthesized powder was calculated by helium-gas pycnometry (AccuPyc 1330, GA, Micromeritics, USA). Thermal gravimetry-differential thermal analysis (TG–DTA, STA) was performed using Simultaneous Thermal Analyser (BÄHR-STA 503) in air. Differential thermal gravimetry (DTG) curves were also demonstrated.

The synthesized Li_2TiO_3 powders were subject to grinding for 4 h at 180 rpm in ethanol using zirconia balls and a planetary mill in order to break hard agglomerates. The slurries were then dried, granulated using 5 Wt% of PVA and uniaxially pressed into pellets under a pressure of 200 MPa. The samples were sintered in an electrical muffle furnace at ambient atmosphere between 1000 and 1300 °C with heating rate of 10 °/min and for 3 h holding time at maximum temperature. The densities were measured by Archimedes method (ASTM C373 standard test method). The relative density was calculated by dividing the Archimedes density over theoretical density. The theoretical density of samples was achieved after crushing the pellets and then measuring the powder density by helium-gas pycnometry. Both LEBM and HEBM-5 powder densities were measured 3.40 g/cm^3. The X-Ray Diffraction (XRD) patterns of powders and pellets were obtained by Philips PW 3710 with Cu-k_α line of 1.5406 Å (40 kV, 30 mA). The data were collected in the 2θ range of 20–80°. The morphology and microstructure of samples were investigated by means of field emission scanning electron microscope (FE-SEM) (TESCAN MIRA 3 LMU). The microstructural observations were performed on polished and thermally etched samples. Thermal etching was performed for each sintered sample at 50 °C below the sintering temperature for 30 min dwell time. Raman spectra have been recorded by DXR-Smart Raman (Thermoscientific) instrument with Smart Excitation Laser (Thermo Scientific) with laser wavelength at 780 nm. Resolution, number of scans and integration time were 2 cm^{-1}, 5 and 1500 s, respectively. Microwave dielectric properties were measured in the frequency range of 8–10 GHz with $TE_{01\delta}$ resonant mode using HP8719C vector network analyzer. The temperature coefficient of resonant frequency τ_f was also measured in the temperature range from 25 to 75 °C.

3 Results and discussion

Figure 1 shows the structural examination of Li_2CO_3 and TiO_2 powder mixtures subject to different high-energy milling times. All peaks are attributed to Li_2CO_3 (JCPDS card number 721216) and TiO_2 (JCPDS card number 211272), while no Li_2TiO_3 or any other phases were identified. The most prominent effect of using high-energy ball milling is peak broadening and intensity reduction which can be attributed to the reduction of crystallite size, loss of long-range periodicity and accumulation of strains in lattice which is accompanied by an increase in the background.

The particle size (D90) of as-received powders are presented in Table 1. As it is obvious, the size of powders has reduced with milling time.

In order to find out the influence of milling on reaction between precursors, they were analyzed by STA (DTA/TG) and the results of LEBM and HEBM-5 powders are presented in Fig. 2.

The DTA curve of LEBM powder with the heating rate of 10 °C/min in Fig. 2b exhibits two overlapping endothermic

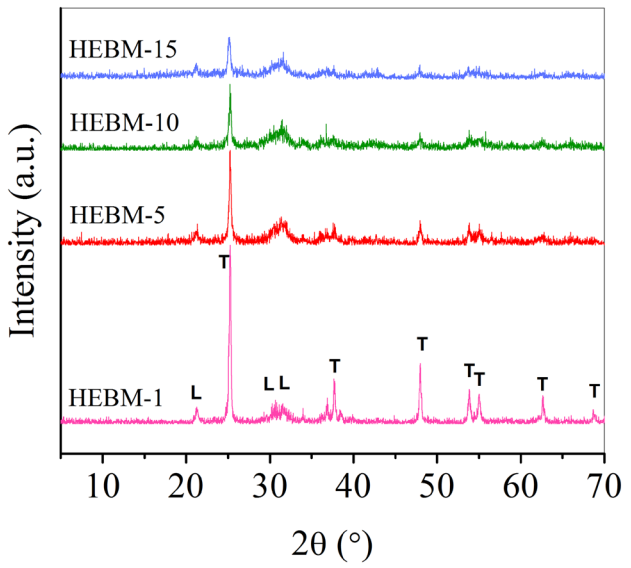

Fig. 1 XRD patterns of HEBM-1, HEBM-5, HEBM-10 and HEBM-15 (L: Li_2CO_3, T: TiO_2)

Table 1 Particle size of powders milled for different durations

Powder	LEBM	HEBM-1	HEBM-5	HEBM-10	HEBM-15
D90 (μm)	3.30	3.09	2.90	2.50	1.96

peaks positioned at around 641 and 706 °C. There exists only one endothermic peak in DTA curve of HEBM-5 powder shown in Fig. 2d at about 592 °C, which is about 50 °C lower than the firs peak in DTA curve of LEBM powder. The first derivative of TG (DTG) graphs presented in Fig. 2a shows that the starting and ending points for the decomposition of Li_2CO_3 in LEBM powder happens at around 511 and 768 °C, respectively, and in HEBM-5 powder reduce to around 354 and 709 °C, respectively. The reduction of decomposition temperature in HEBM-5 powder reveals that the CO_2 gas escapes at lower temperature by milling process followed by increasing specific surface area of starting powders. Since as reported in [39] the reaction between Li_2CO_3 and TiO_2 starts from the surface of particles and with increase in powder surface area more active sites for reaction develop. The results of estimated area under DTA peaks of LEBM and HEBM-5 powders (Fig. 2b, d) are 2623 and 1921 respectively which shows that the milling process decreases the heat of formation of Li_2TiO_3 (about 26%) as well as the reaction temperature between starting precursors.

The mixture of starting powders (LEBM) was annealed at 600 °C without any holding time and the XRD patterns of the powder as well as XRD patterns of starting materials are shown in Fig. 3. Patterns show the existence of all three phases of Li_2CO_3, TiO_2 and Li_2TiO_3 that determines the broad endothermic peak to be related to the reaction between starting powders as explained by Eq. (2) and the release of CO_2 happens simultaneously along with Li_2TiO_3 formation:

$$Li_2CO_3 + TiO_2 \rightarrow Li_2TiO_3 + CO_2 \quad (2)$$

The second peak in Fig. 2b may be related to the melting of remaining Li_2CO_3 as the transformation temperature is close to melting point of Li_2CO_3 ($T_m = 740$ °C [43–45]).

Figure 4 illustrates the room temperature XRD patterns of LEBM and HEBM-5 powders annealed at different temperatures of 500, 550, 600, 700 and 800 °C for 4 h. All existing peaks in samples annealed at 700 and 800 °C are related to monoclinic β-Li_2TiO_3 (JCPDS card: 330,831) without any additional phases. Increasing the temperature causes the increase of peak intensities of superstructure due to higher order of crystallinity, while the width of peaks become narrower due to crystallite growth. Based on the results of phase analysis taken from synthesized powders presented in Fig. 4 the calcination temperature of 700 °C were adopted for the rest of research as no additional phases were observed.

SEM micrographs of Li_2TiO_3 powders synthesized via two different processes (LEBM and HEBM-5) are demonstrated in Fig. 5. Figure 5a reveals the presence of hard agglomerates with non-spherical morphology related to LEBM powder particles, while Fig. 5b shows different morphology and particle size of HEBM-5 powders with spherical morphology and measured particle size of 147 ± 45 nm. The surface area of this powder was measured to be 15.75 m^2/g and based on Eq. (1) the particle size was obtained to be 115 nm in fair agreement with SEM observations.

Green density of LEBM pellets was calculated to be 60% of the theoretical density which increased to 65% after high-energy mill. Figure 6a shows the results of density measurements of HEBM-1, HEBM-5, HEBM-10 and HEBM-15 sintered at 1100 °C. Increasing the milling time from 1 to 5 h enhances the density from 3.11 to 3.19 g/cm^3 which remains almost unchanged adopting higher milling durations. Figure 6b illustrates the density variation of HEBM-5 sample with respect to temperature as well as LEBM. HEBM-5 sample reaches the maximum density of 3.19 g/cm^3 at sintering temperature of 1100 °C that remains almost unchanged at higher sintering temperature of 1200 °C and then decreases at 1300 °C. A similar density (3.18 g/cm^3) is reported in [18] after sintering the nano-size Li_2TiO_3 ceramics prepared via sol–gel method with average particle size of 6–12 nm. The density of LEBM samples enhances with increasing the sintering temperature to 1200 °C ($\rho_{max} = 3.08$ g/cm^3) and reduces with further increasing the temperature. Decreasing the density of both samples at 1300 °C could be due to lithium sublimation. Figure 6b also demonstrates the superiority of sintering behavior of high-energy ball milled parts in comparison with low-energy ball milled parts. Improvement

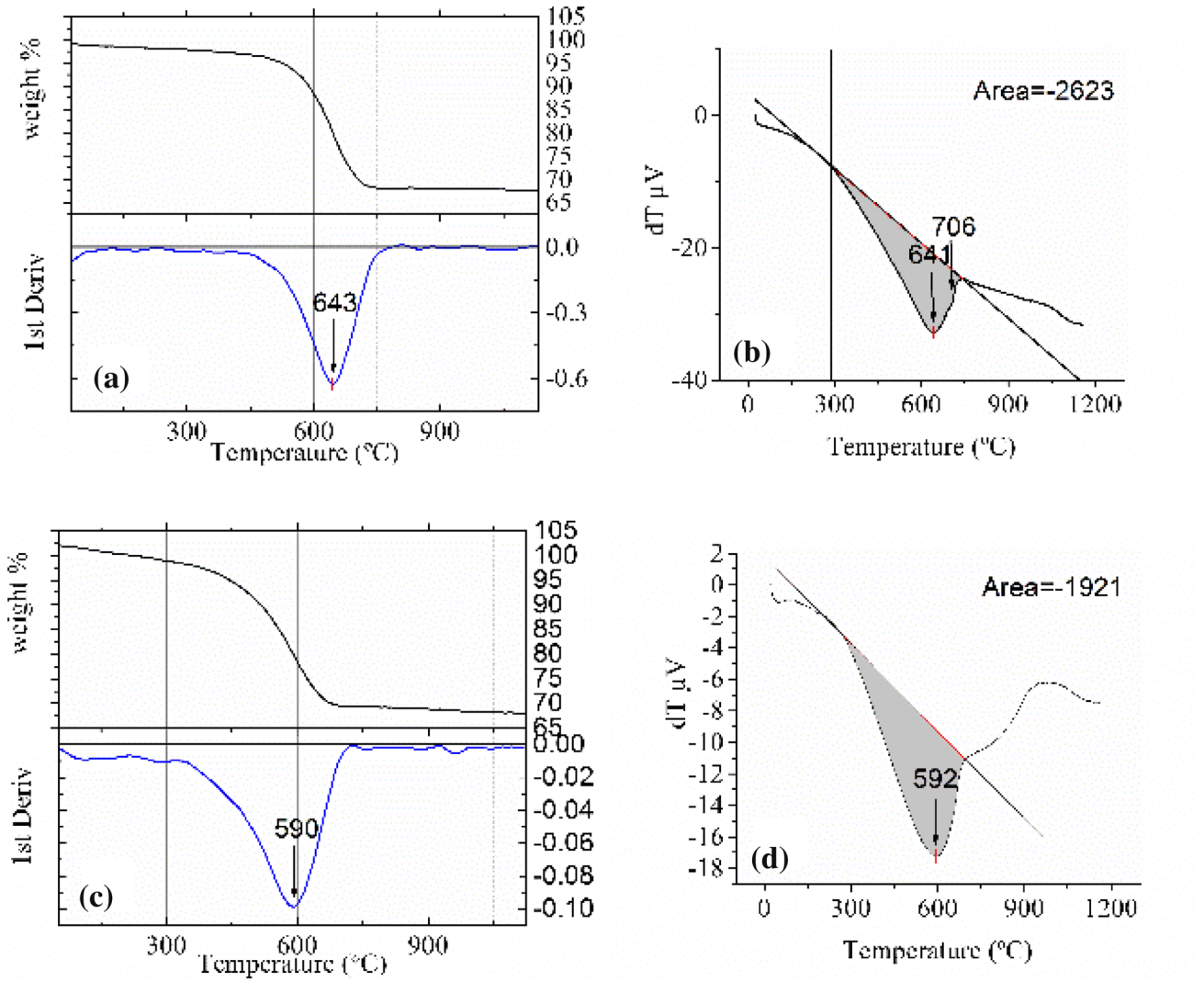

Fig. 2 **a** TG and DTG analysis of LEBM, **b** DTA of LEBM, **c** TG and DTG analysis of HEBM-5, **d** DTA of HEBM-5 with heating rate of 10 °C/min

of density can be explained by high surface area of fine synthesized powders which increases the driving force of sintering.

Figure 7 shows the room temperature XRD patterns of LEBM and HEBM-5 pellets sintered at 1200 °C for 3 h. Both patterns include peaks related to the monoclinic phase of Li_2TiO_3.

Raman spectra of sintered pellets are presented in Fig. 8 and the spectra are very similar and verify the phase purity of samples. In Li_2TiO_3, the frequencies within 700–550, 400–550, and 250–400 cm^{-1} region are assigned to Ti–O stretching in TiO_6 octahedral, Li–O stretching in tetrahedral, and Li–O stretching in octahedral coordinations respectively. In the Li_2TiO_3 structure, the lithium can occupy both octahedral and tetrahedral positions [46, 47]. Lorentzian functions were employed to deconvolute the spectra into different modes of vibration (Fig. 9) and the FWHM of different peaks are presented in Table 2.

Comparing the FWHM bands located at 658, 419 and 348 cm^{-1} in two samples reveals the higher value in HEBM rather than LEBM which can be due to lower crystallinity of the HEBM-5 sample.

The SEM micrographs of thermal-etched LEBM and HEBM-5 samples sintered at different temperatures are illustrated in Fig. 10. SEM images of LEBM samples sintered at all temperatures exhibit a finer microstructure containing grains within a narrow range of size in comparison with HEBM-5 pellets sintered at the same temperatures albeit HEBM-5 powders possess fine particle size due to mechanochemical effect. The grain size of LEBM and HEBM-5 ceramics sintered at 1100 °C were calculated 4.16 ± 0.38 and 9.16 ± 1.89 µm, respectively.

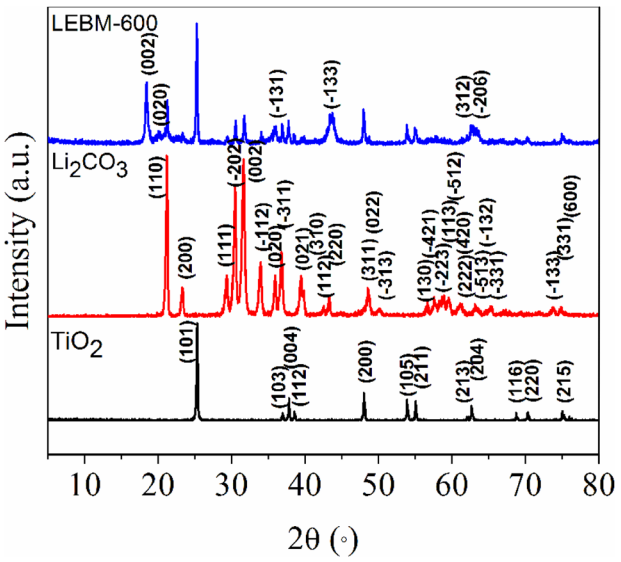

Fig. 3 XRD patterns of LEBM powders annealed at 600 °C without holding time along with starting materials

SEM micrographs of the HEBM-5 samples indicate the occurrence of abnormal grain growth. The same result is reported in [18] after sintering of Li_2TiO_3 powders with particle size in the range of 6–12 nm and is believed to be responsible for deteriorated quality factor of ceramic. Preferential orientation of grain growth is observed in all microstructures after sintering at higher temperatures of 1200 and 1300 °C. The presence of micro-cracks due to order–disorder transition and micro-pores due to lithium sublimation are also obvious at higher temperatures.

Figure 11a, b show the microwave dielectric properties of the LEBM and HEBM-5 ceramics sintered at different temperatures. HEBM parts possess higher ε_r value at all temperatures with maximum value of 21.8 obtained at 1100 °C. The superiority of ε_r in HEBM-5 over LEBM is in agreement with the superiority of its bulk density as shown in Fig. 6 and can be explained by Clausius–Mossotti equation. Based on this equation the dielectric constant of ceramic is controlled by the dipoles present in unit cell volume and dielectric polarizabilities of ions [19, 48]. The higher the density of ceramic, the higher the dipoles in a unit cell volume and therefore the higher the value of ε_r [19, 20, 49]. The relation can also be explained because of the unity of ε_r of air [18].

From Fig. 11b it can be observed that quality factor tends to decreases using high-energy mill. The reason can be attributed to the microstructure showing abnormal grain growth (Fig. 10) or lower crystallinity of samples proved by Raman technique (Table 1). The $Q \times f$ value of HEBM ceramic increases with increasing temperature up to 1100 °C and then decreases at higher temperatures but the maximum quality factor of LEBM parts was measured at 1200 °C. The temperature variation of resonant frequency τ_f of HEBM-5 parts sintered at 1100 and 1200 °C were measured + 26 ppm/°C.

4 Conclusion

Reaction mechanism for the synthesis of Li_2TiO_3 from the mixture of Li_2CO_3 and TiO_2 were investigated by means of DTA/TG and XRD procedures which proved milling

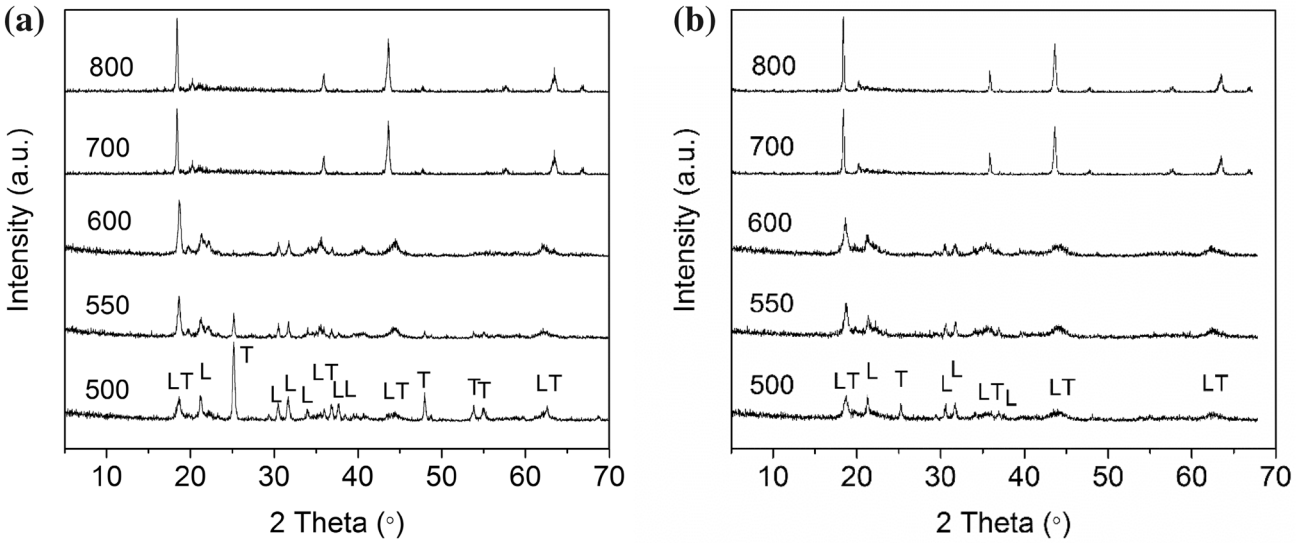

Fig. 4 XRD patterns of **a** LEBM and **b** HEBM-5 powders annealed at 500, 550, 600, 700 and 800 °C with a holding time of 4 h (LT: Li_2TiO_3, L: Li_2CO_3, T: TiO_2)

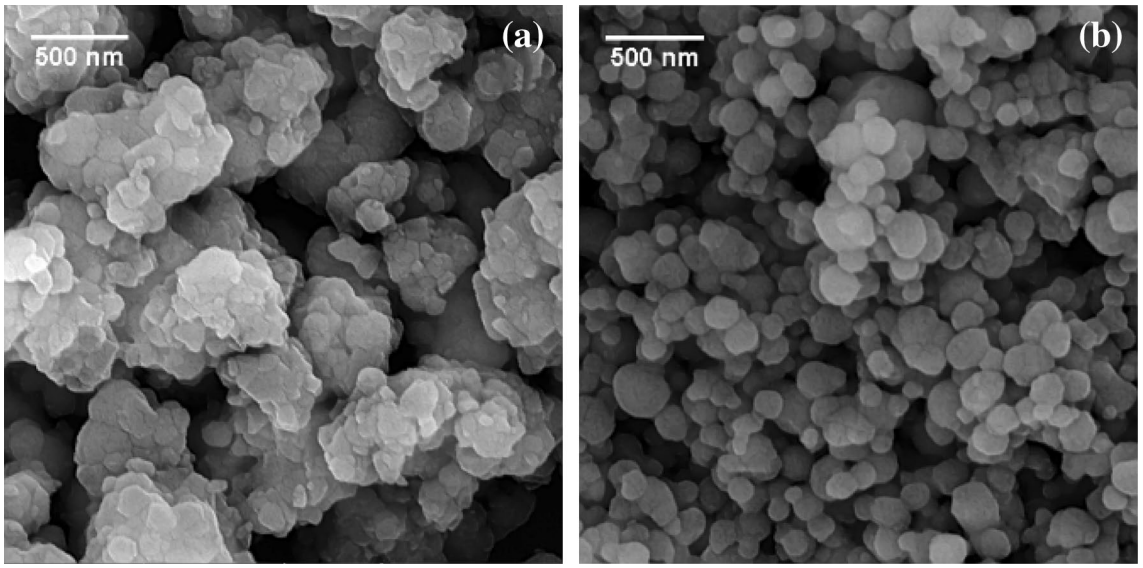

Fig. 5 Morphology of **a** LEBM and **b** HEBM-5 powders calcined at 700 °C

Fig. 6 **a** Density of high-energy ball milled samples for different milling times of 1, 5, 10, 15 (HEBM-1, HEBM-5, HEBM-10, HEBM-15) sintered at 1100 °C and **b** density of LEBM and HEBM-5 specimens sintered at different temperatures for 3 h

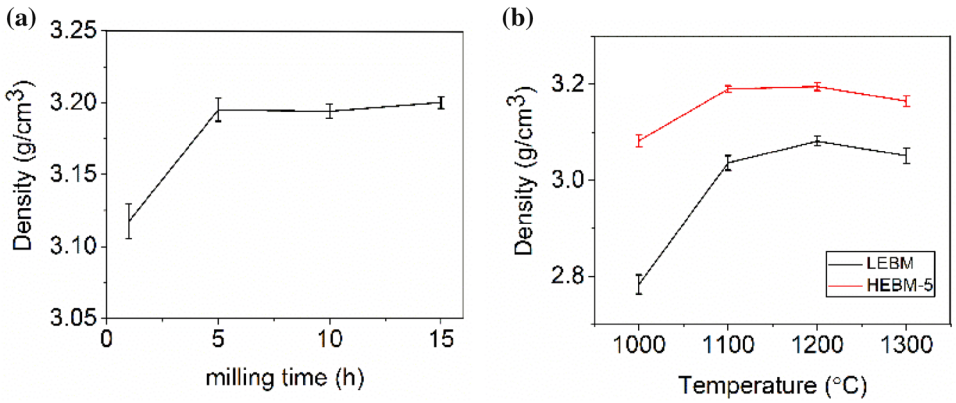

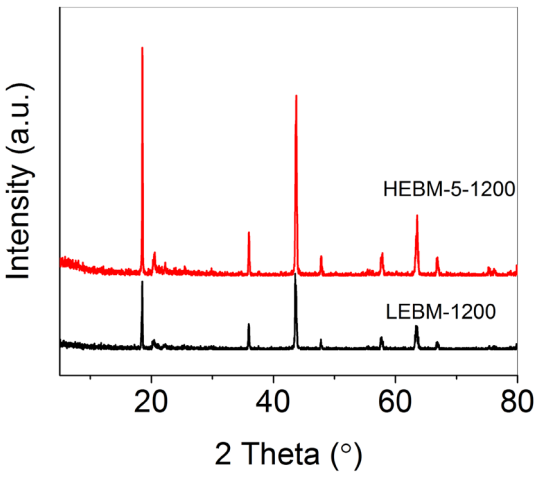

Fig. 7 XRD patterns of LEBM and HEBM-5 samples sintered at 1200 °C for 3 h (all peaks attributed to monoclinic β-Li_2TiO_3 (JCPDS card: 330831))

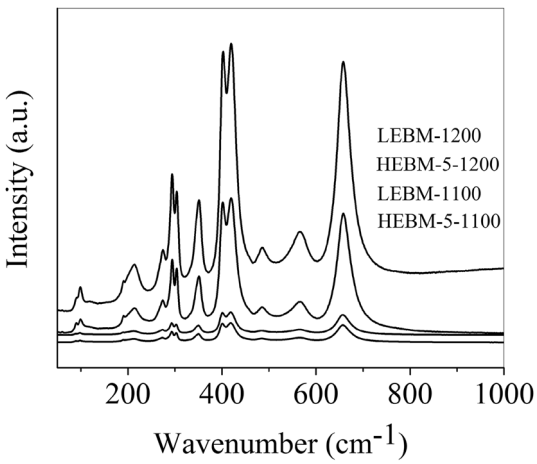

Fig. 8 Raman spectra of LEBM and HEBM sintered at 1100 and 1200 °C

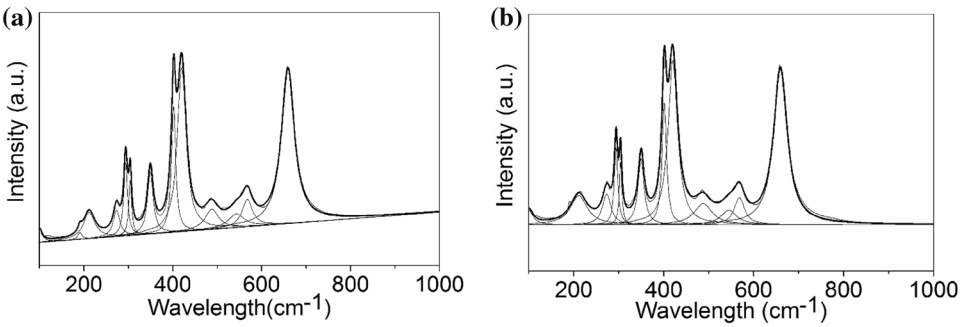

Fig. 9 Deconvoluted Raman spectra of **a** LEBM and **b** HEBM-5 sintered at 1200 °C into different modes of vibration

Table 2 FWHM of Raman peaks located at 658, 419 and 348 cm^{-1}

Specimen	FWHM (658)	FWHM (419)	FWHM (348)
LEBM-1200	34.93	23.80	15.44
HEBM-1200	36.52	25.63	16.56

process decreases both the reaction temperature between starting precursors (about 60 °C) and the heat of formation of Li_2TiO_3 (about 26%). Fine Li_2TiO_3 powders (< 200 nm) were synthesized through high-energy ball mill for 5 h and these powders had higher sinterability because of the resultant high surface area. The maximum value of $\varepsilon_r = 21.85$ is obtained through density increase resulting from fine particle size. The SEM investigations of sintered pellets showed that abnormal grain growth occurred in high-energy milled sample that could be the reason for deteriorated $Q \times f$ of the ceramic. The temperature variations of resonant frequency τ_f of ceramic sintered at 1100 °C was measured + 26 ppm/°C.

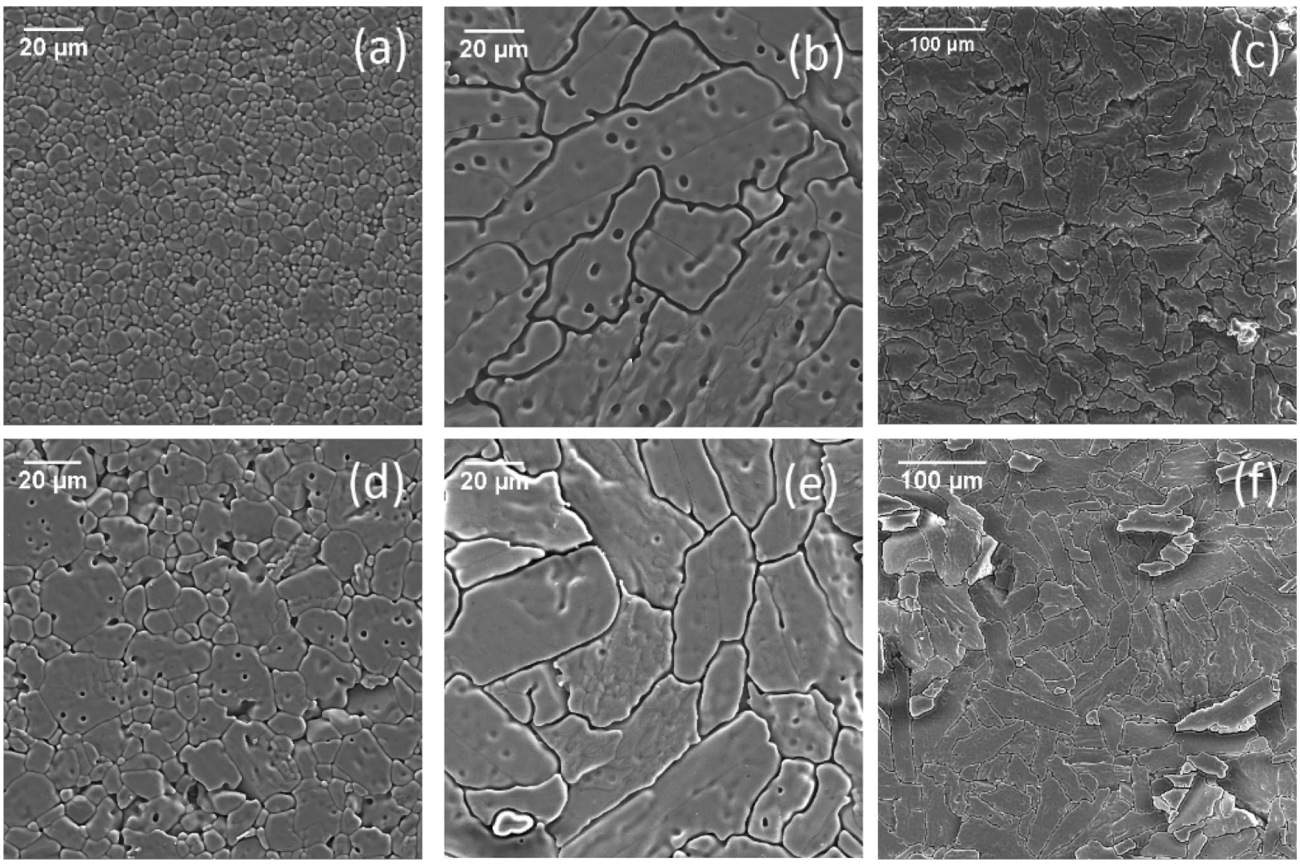

Fig. 10 SEM micrographs of LEBM ceramic sintered at **a** 1100 °C, **b** 1200 °C, **c** 1300 °C and HEBM-5 ceramic sintered at **d** 1100 °C, **e** 1200 °C, **f** 1300 °C

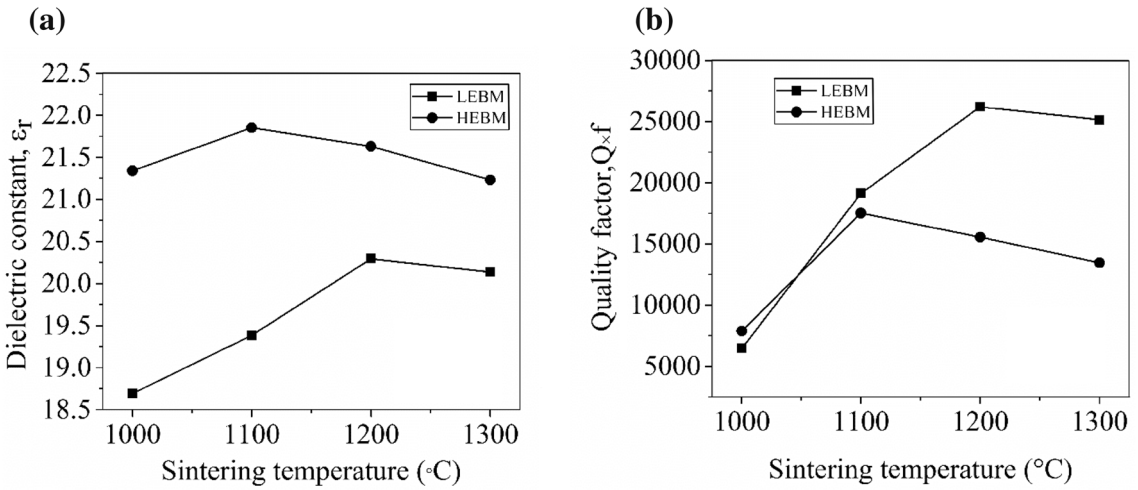

Fig. 11 **a** Dielectric constant and **b** Q×f of LEBM and HEBM-5 versus the sintering temperature

References

1. W. Hu et al., Microstructure and microwave dielectric properties of TiO_2-doped pseudo-wollastonite ceramics. J. Mater. Sci.: Mater. Electron. **25**(11), 4730–4734 (2014)
2. Y. Wang et al., Sintering behavior and microwave dielectric properties of Li_2O–B_2O_3–SiO_2 doped $MgTiO_3$–$CaTiO_3$ ceramics. J. Mater. Sci.: Mater. Electron. **26**(7), 4963–4968 (2015)
3. X. Lu et al., Effects of ZnO additive on crystalline phase and microwave dielectric properties of 0.90 Al_2O_3–0.10 TiO_2 ceramics. J. Mater. Sci.: Mater. Electron. **27**(3), 2687–2692 (2016)
4. J. Shen, J. Zhang, N. Xu, MnO_2 on eliminating Al_2TiO_5 and promoting microwave dielectric properties of 0.90 Al_2O_3–0.10TiO_2 composite ceramics. J. Mater. Sci.: Mater. Electron. **29**, 1–6
5. T. Guo et al., $SrZn_2(PO_4)_2$–TiO_2 composite microwave dielectric ceramics with wide tunability range for temperature coefficient of resonant frequency. J. Mater. Sci.: Mater. Electron. **28**, 1–6 (2017)
6. J.X. Bi et al., Correlation of crystal structure and microwave dielectric properties of $Zn_{1-x}Ni_xZrNb_2O_8$ ($0 \le x \le 0.1$) ceramics. J. Alloy Compd. **727**, 123–134 (2017)
7. M.T. Sebastian, R. Ubic, H. Jantunen, Low-loss dielectric ceramic materials and their properties. Int. Mater. Rev. **60**(7), 392–412 (2015)
8. J. Song et al., Microstructure characteristics and microwave dielectric properties of calcium apatite ceramics as microwave substrates. J. Alloy Compd. **731**(Supplement C): 264–270 (2018)
9. X. Yang et al., Phase structures and microwave dielectric properties of $xCaTiO_3$–$(1–x)Sm_{0.9}Nd_{0.1}AlO_3$ ceramics. J. Mater. Sci.: Mater. Electron. **24**(11), 4662–4668 (2013)
10. G. Yao, P. Liu, H. Zhang, Microwave dielectric properties of $Li_2MgTi_3O_8$ ceramics produced by reaction-sintering method. J. Mater. Sci.: Mater. Electron. **24**(4), 1128–1131 (2013)
11. C.-L. Huang, Y.-W. Tseng, J.-Y. Chen, High-Q dielectrics using ZnO-modified Li_2TiO_3 ceramics for microwave applications. J. Eur. Ceram. Soc. **32**(12), 3287–3295 (2012)
12. D. Zhou et al., Microwave dielectric characterization of a Li_3NbO_4 ceramic and its chemical compatibility with silver. J. Am. Ceram. Soc. **91**(12), 4115–4117 (2008)
13. J.J. Bian, L. Wang, L.L. Yuan, Microwave dielectric properties of $Li_{2+x}Ti_{1-4x}Nb_{3x}O_3$ ($0 \le x \le 0.1$). Mater. Sci. Eng. B **164**(2), 96–100 (2009)
14. L.X. Pang, D. Zhou, Microwave dielectric properties of low-firing Li_2MO_3 (M = Ti, Zr, Sn) ceramics with B_2O_3–CuO addition. J. Am. Ceram. Soc. **93**(11), 3614–3617 (2010)
15. L.L. Yuan, J.J. Bian, Microwave dielectric properties of the lithium containing compounds with rock salt structure. Ferroelectrics **387**(1), 123–129 (2009)
16. J.J. Bian, Y.F. Dong, New high Q microwave dielectric ceramics with rock salt structures: $(1–x)Li_2TiO_3 + xMgO$ system ($0 \le x \le 0.5$). J. Eur. Ceram. Soc. **30**(2), 325–330 (2010)
17. M.R.D. Khaki et al., Evaluating the efficiency of nano-sized Cu doped TiO_2/ZnO photocatalyst under visible light irradiation. J. Mol. Liq. **258**, 354–365 (2018)
18. Y. Hao et al., Enhanced sintering characteristics and microwave dielectric properties of Li_2TiO_3 due to nano-size and nonstoichiometry effect. J. Mater. Chem. **22**(45), 23885 (2012)
19. Y.-Z. Hao et al., Microwave dielectric properties of Li_2TiO_3 ceramics doped with LiF for LTCC applications. J. Alloy Compd. **552**, 173–179 (2013)
20. J. Liang et al., A new route to improve microwave dielectric properties of low-temperature sintered Li_2TiO_3-based ceramics. J. Mater. Sci.: Mater. Electron. **24**(10), 3625–3628 (2013)
21. J.J. Bian, Y.F. Dong, Sintering behavior, microstructure and microwave dielectric properties of $Li_{2+x}TiO_3$ ($0 \le x \le 0.2$). Mater. Sci. Eng. B **176**(2), 147–151 (2011)
22. M.R.D. Khaki et al., Enhanced UV–Visible photocatalytic activity of Cu-doped ZnO/TiO_2 nanoparticles. J. Mater. Sci.: Mater. Electron. **29**(7), 5480–5495 (2018)
23. J. Wang et al., Low-temperature sintered Zn $(Nb_{1-x}V_{x/2})_2O_{6–2.5x}$ microwave dielectric ceramics with high Q value for LTCC application. J Alloys Compd **392**(1), 263–267 (2005)
24. J. Zhang, Y. Zhou, Z. Yue, Low-temperature sintering and microwave dielectric properties of LiF-doped $CaMg_{1-x}Zn_xSi_2O_6$ ceramics. Ceram. Int. **39**(2), 2051–2058 (2013)
25. J. Pei et al., Microwave dielectric ceramics of hexagonal $(Ba_{1-x}A_x)La_4Ti_4O_{15}$ (A = Sr, Ca) for base station applications. J. Alloys Compd. **459**(1), 390–394 (2008)
26. X.-J. Bai et al., Low-temperature sintering and microwave dielectric properties of LiF-doped $Ba(Mg_{1/2}W_{1/2})O_3$–TiO_2 ceramics. J. Alloys Compd. **667**, 146–150 (2016)
27. A. Sayyadi-Shahraki et al., Microwave dielectric properties and chemical compatibility with silver electrode of Li_2 TiO_3

ceramic with Li_2O–ZnO–B_2O_3 glass additive. Physica B **457**, 57–61 (2015)
28. J. Liang, W.-Z. Lu, Microwave dielectric properties of Li_2TiO_3 ceramics doped with ZnO-B_2O_3Frit. J. Am. Ceram. Soc. **92**(4), 952–954 (2009)
29. J. Liang et al., Microwave dielectric properties of Li_2TiO_3 ceramics sintered at low temperatures. Mater. Sci. Eng. B **176**(2), 99–102 (2011)
30. S.R. Pouran et al., Effects of niobium and molybdenum impregnation on adsorption capacity and Fenton catalytic activity of magnetite. RSC Adv. **5**(106), 87535–87549 (2015)
31. A. Houshmand, W.M.A.W. Daud, M.S. Shafeeyan, Tailoring the surface chemistry of activated carbon by nitric acid: study using response surface method. Bull. Chem. Soc. Jpn. **84**(11), 1251–1260 (2011)
32. C. Hu, P. Liu, Preparation and microwave dielectric properties of SiO_2 ceramics by aqueous sol–gel technique. J. Alloy Compd. **559**, 129–133 (2013)
33. H. Wang et al., Synthesis and microwave dielectric properties of $CaSiO_3$ nanopowder by the sol–gel process. Ceram. Int. **34**(6), 1405–1408 (2008)
34. B. Guo et al., Microwave dielectric properties of Li_2MgTiO_4 ceramics synthesized via high energy ball milling method. Ferroelectrics **494**(1), 123–130 (2016)
35. L. Cheng et al., Microwave dielectric properties of Mg_2TiO_4 ceramics synthesized via high energy ball milling method. J. Alloy Compd. **623**, 238–242 (2015)
36. S.R. Pouran et al., Comprehensive study on the influence of molybdenum substitution on characteristics and catalytic performance of magnetite nanoparticles. Res. Chem. Intermediat. **44**(2), 883–900 (2018)
37. S.R. Pouran et al., Ultrasound and UV assisted Fenton treatment of recalcitrant wastewaters using transition metal-substituted-magnetite nanoparticles. J. Mol. Liq. **222**, 1076–1084 (2016)
38. F. Rubio-Marcos et al., Effect of stoichiometry and milling processes in the synthesis and the piezoelectric properties of modified KNN nanoparticles by solid state reaction. J. Eur. Ceram. Soc. **30**(13), 2763–2771 (2010)
39. N. Duc Van, Effects of processing parameters on the synthesis of ($K_{0.5}Na_{0.5}$) NbO_3 nanopowders by reactive high-energy ball milling method. Sci. World J. 2014. https://doi.org/10.1155/2014/203047
40. I. Veljković et al., Solid state synthesis of extra phase-pure $Li_4Ti_5O_{12}$ spinel. Sci. Sinter. **43**(3), 343–351 (2011)
41. Y. Shen et al., Solid state formation mechanism of $Li_4Ti_5O_{12}$ from an anatase TiO_2 source. Chem. Mater. **26**(12), 3679–3686 (2014)
42. A. Shamiri et al., Experimental and modeling analysis of propylene polymerization in a pilot-scale fluidized bed reactor. Ind. Eng. Chem. Res. **53**(21), 8694–8705 (2014)
43. A. Shamiri et al., Absorption of CO_2 into aqueous mixtures of glycerol and monoethanolamine. J. Nat. Gas Sci. Eng. **35**, 605–613 (2016)
44. M.S. Shafeeyan et al., Modification of activated carbon using nitration followed by reduction for carbon dioxide capture. Bull. Korean Chem. Soc. **36**(2), 533–538 (2015)
45. D. Mandal, D. Sathiyamoorthy, V.G. Rao, Preparation and characterization of lithium–titanate pebbles by solid-state reaction extrusion and spherodization techniques for fusion reactor. Fusion Eng. Des. **87**(1), 7–12 (2012)
46. R.Yusoff et al., Physical properties of aqueous mixtures of N-methyldiethanolamine (MDEA) and ionic liquids. J. Ind. Eng. Chem. **20**(5), 3349–3355 (2014)
47. T. Nakazawa et al., High energy heavy ion induced structural disorder in Li_2TiO_3. J. Nucl. Mater. **367**, 1398–1403 (2007)
48. S.R. Pouran et al., A comparative study on a cationic dye removal through homogeneous and heterogeneous Fenton oxidation systems. Acta Chim. Slov. **65**(1), 166–171 (2018)
49. A. Shamiri et al., Dynamic modeling of gas phase propylene homopolymerization in fluidized bed reactors. Chem. Eng. Sci. **66**(6), 1189–1199 (2011)